Analysis of the Steady-State Current Ripple in Multileg Class-D Power Amplifiers Under Inductance Mismatches

Xudong Wang, *Student Member, IEEE*, Zhengming Zhao, *Fellow, IEEE*, Kai Li, *Member, IEEE*, Kainan Chen, *Member, IEEE*, and Fang Liu, *Student Member, IEEE*

***Abstract*—Multileg Class-D amplifiers (CDAs) with phase-shifted carrier modulation can increase the equivalent switching frequency and reduce the output current ripples, which further reduces the size of the output filter. However, these benefits are degraded by the tolerances in the phase inductance values. The phase inductance mismatches impact the ripple cancelation effects (the harmonic contents at switching frequency and its harmonics appearing in the output current ripple). Therefore, the quality of the output waveform can further be impacted. Current research works dealing with this issue mainly focused on the interleaved dc–dc converters, which does not cover the analysis in multileg CDAs or inverters, especially for the full-bridge configuration. This paper proposes a general analytical method to characterize the steady-state phase and the total current ripple in the multileg CDAs with full-bridge configuration under inductance mismatches. Monte Carlo simulation is used to study the impact of inductance mismatches on the harmonic contents of the total current ripple, and the distribution law of the inductances at the worst case is revealed. The analytical method is verified by simulation and experimental results of a four-leg full-bridge CDA. A design guideline is given to optimize the filter design based on the analytical method.**

***Index Terms*—Class-D amplifiers (CDAs), current ripples, inductance mismatches.**

I. Introduction

HIGH-POWER Class-D amplifiers (CDAs) have been studied for the applications that require high switching frequency and high-power handling capability, such as industrial vibration test systems, electromagnetic interference test systems, and current control systems for magnetic resonance imaging scanners [1], [2]. Compared to the traditional linear power amplifiers, the main drawback of CDAs is the low bandwidth due to the limitation of the switching frequency of the power semiconductor devices. To overcome this drawback, the phase-shifted carrier modulation (PSCM) has been used in CDAs [3], which can be regarded as the multileg (multiphase) interleaved dc–ac converters. The double Fourier series analysis [4] has revealed that PSCM can reduce the harmonic components at the switching frequency and its harmonics at the output, and increase the output bandwidth without increasing the switching frequency [3], [5]. Another advantage of PSCM is the ripple reduction of the total current, which also reduces the output capacitance [6].

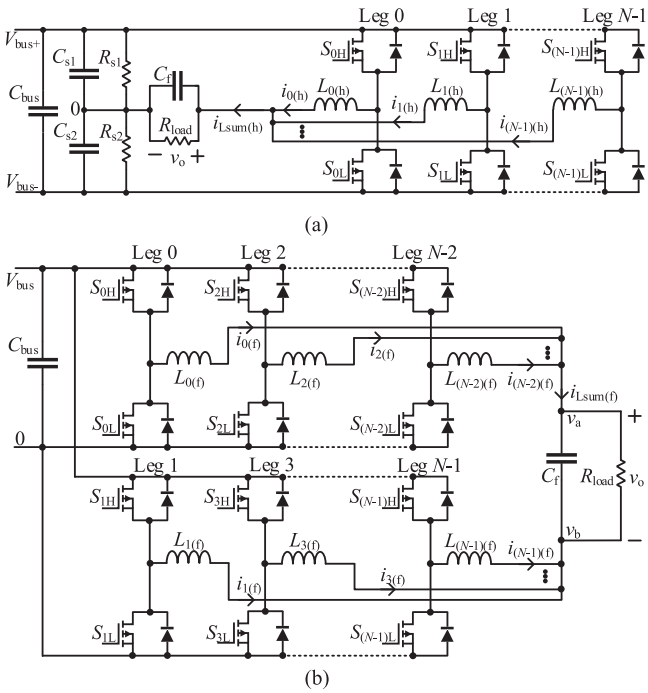

Fig. 1. General topology of multileg CDA. (a) MHB CDAs. (b) MFB CDAs.

The general topology of the multileg CDA is shown in Fig. 1(a). Balanced topology shown in Fig. 1(b) can be used when the number of legs in parallel is even [3]. This paper uses the abbreviation MHB CDAs (Multileg Half-Bridge CDAs) for the topology in Fig. 1(a) and MFB CDAs (Multileg Full-Bridge CDAs) for the topology in Fig. 1(b). Also, for the variables in the later derivations, (f) and (h) in the subscripts refer to MFB and MHB CDAs, respectively. The total current ripple refers to the current ripple of $i_{L\mathrm{sum(h)}}$ for MHB CDAs and $i_{L\mathrm{sum(f)}}$ for MFB CDAs, as shown in Fig. 1. Compared to the MHB CDAs,

Manuscript received February 23, 2018; accepted June 14, 2018. Date of publication June 26, 2018; date of current version February 20, 2019. This work was supported by the Major Program of National Natural Science Foundation of China under Grant 51490683. Recommended for publication by Associate Editor R. C. N. Pilawa-Podgurski. *(Corresponding author: Zhengming Zhao.)*

The authors are with the Department of Electrical Engineering, Tsinghua University, Beijing 100084, China (e-mail:

there is no need for a neutral point in MFB CDAs. Also, due to the bridge-tied load (BTL) configuration, the dc bus voltage of MFB CDAs can be halved compared to that of MHB CDAs. Therefore, the breakdown voltage requirement of the power semiconductor switches is halved for MFB CDAs.

However, some practical issues affecting the aforementioned features of multileg interleaved converters, should be considered, such as the tolerances and nonidealities of passive and active components [7]–[9]. A major effect is the imbalance of dc current distribution among phases, which can be solved by digital control techniques [10]–[12]. The mismatches of phase inductance values mainly influence the peak values of the phase current ripples and the ripple cancelation effect, which, however, cannot be removed by control strategies [13]. The tolerance of the inductance values can vary up to $\pm 15\%$, caused by the tolerance in the manufacture process and the magnetic property variations [6]. To study the effects of inductance mismatches, the information of the phase current ripple is needed, which is assumed as a triangular wave for interleaved converters [13], [14].

The input current and output voltage spectrums of the half-bridge and full-bridge inverters have been studied analytically in [15]. However, the multileg inverter is not considered. The established analytical method to characterize the current ripple in interleaved converters can be directly applied to MHB CDAs. However, for MFB CDAs, the phase current ripple cannot be regarded as a triangular wave, which, in fact, cannot have a uniform and simple characterization. The reason is that the output voltages at the common point of the legs in balanced topology v_a and v_b [as shown in Fig. 1(b)] change with the switching states of all the legs. While for the half-bridge configuration, the output voltage at the common point equals to v_o and can be assumed as constant during a switching cycle. As v_a and v_b change with the switching functions of all the legs, the waveform of $i_{x(\mathrm{f})}$ depends on the switching sequence of all the legs. Fig. 2 shows the simulation waveforms of $i_{x(\mathrm{f})}$ during the switching period *T* when the total phase number is four, with different switching sequence according to the duty ratio *D*. It can be found that the waveform of $i_{x(\mathrm{f})}$ is no more a triangular wave and cannot have a simple and uniform characterization.

Therefore, it becomes a complicated work to directly follow the analysis given in [13] and [14] for MFB CDAs. Considering the advantages of using the full-bridge topology over the half-bridge topology for CDAs and inverters, it is necessary to analyze the current ripple in MFB CDAs under inductance mismatches. To the best knowledge of the authors, no effective solution to this problem has been proposed.

This paper proposes a general analytical method to characterize the phase and total current ripple in MFB CDAs under inductance mismatches. Theoretical analysis proves that the characterization of the phase current ripple in MFB CDAs can be characterized by a linear combination of the phase current ripple in MHB CDAs. Thus, a simple and uniform time-domain analysis on the current ripple in MFB CDAs is derived. Then, the worst case of the effects on the total current ripple harmonics when the inductor values vary within the tolerance limits is analyzed by Monte Carlo simulation. Furthermore, the influence of the inductance mismatches on the total current ripple and its harmonics is studied analytically and verified by the simulation and experimental results. Finally, a design guideline is given to optimize the design of the output filter considering the phase inductance mismatches.

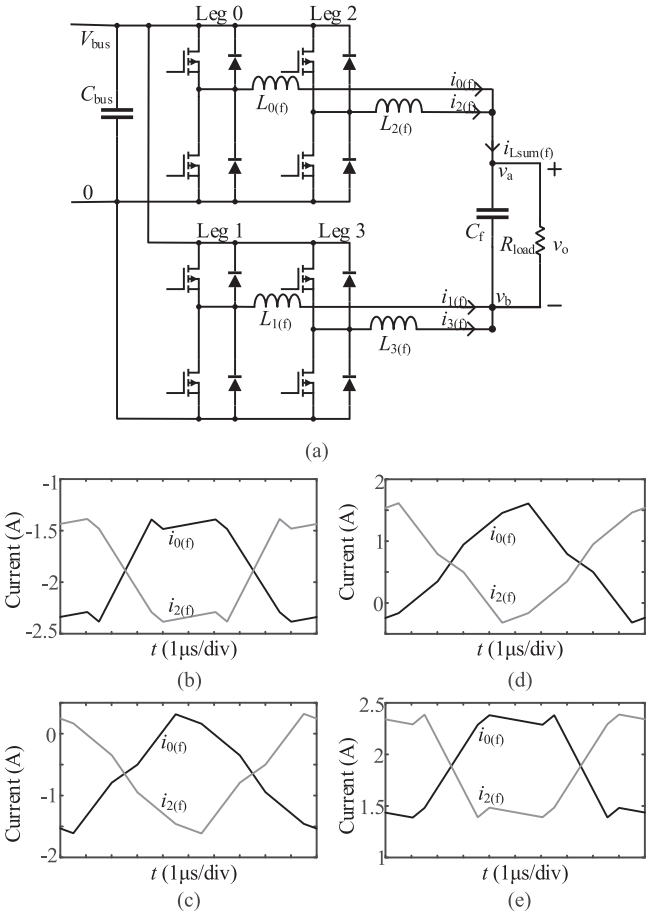

Fig. 2. Simulation waveforms of $i_{0(\mathrm{f})}$ and $i_{2(\mathrm{f})}$ when the total phase number is four. ($V_{\mathrm{bus}} = 200$ V, $R_{\mathrm{load}} = 30\,\Omega$, and $T = 10$ μs.) (a) MFB CDAs with 4 legs. (b) $D = 0.2$. (c) $D = 0.4$. (d) $D = 0.6$. (e) $D = 0.8$.

II. Theoretical Analysis

This section will first introduce the modulation principle of MHB and MFB CDAs, which implies that the inductor current ripples in MFB CDAs are related to that in MHB CDAs. Therefore, the characterization of current ripples in MFB CDAs can be solved by utilizing this relationship. Inspired by this idea, Section II-B will first introduce the established characterization of current ripple in MHB CDAs, which is the basis for later derivations. Then, the relationship between MFB CDAs and MHB CDAs is introduced in Section II-C, and the characterization of current ripple in MFB CDAs is given. Further, the harmonic analysis of the current ripple is given in Section II-D.

A. Modulation Principle of MFB CDAs

Fig. 3 shows the modulation principle for MHB and MFB CDAs [16]. $V_{r(\mathrm{h})}$ and $V_{r(\mathrm{f})}$ are the reference signal of MHB and MFB CDAs, respectively. $V_{\mathrm{tri}x(\mathrm{h})}$ and $V_{\mathrm{tri}x(\mathrm{f})}$ are the triangle

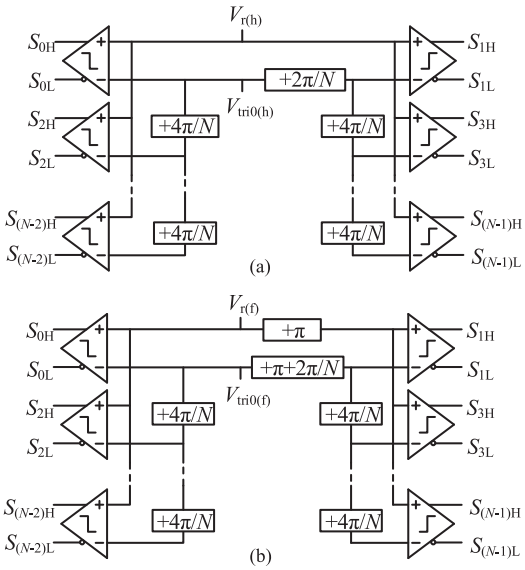

Fig. 3. Modulation principle of (a) MHB CDAs and (b) MFB CDAs [16].

carrier signal of leg x in MHB and MFB CDAs, respectively. For MHB CDAs, the phase shift angle among all legs is $2\pi/N$, where N is the total number of legs. For MFB CDAs, the modulation principle in Fig. 3(b) ensures that the switch action (turn-ON or turn-OFF) of the same leg in MHB and MFB CDAs happens simultaneously with the same reference signal, which is further verified by the modulation waveforms when the leg number is four, as shown in Fig. 4.

As shown in Fig. 4, $V_{r(h)}$ and $V_{r(f)}$ are the same reference signal. $V_{pwmx(h)}$ and $V_{pwmx(f)}$ are the output pulsewidth modulation (PWM) signals of leg x. $V_{pwmo(h)}$ and $V_{pwmo(f)}$ are the equivalent output PWM signals. According to the modulation principle shown in Fig. 3, the phase angle of $V_{tri0(f)}$ and $V_{tri2(f)}$ are identical to $V_{tri0(h)}$ and $V_{tri2(h)}$, while $V_{tri1(f)}$ and $V_{tri3(f)}$ have a phase shift of π, compared to $V_{tri1(h)}$ and $V_{tri3(h)}$. The PWM signals $V_{pwmx(h)}$ and $V_{pwmx(f)}$ verify that the switching instants of leg x in MHB and MFB CDAs are identical. Therefore, the equivalent output PWM signals are the same between MHB and MFB CDAs.

B. Characterization of Current Ripple in MHB CDAs

The MHB CDAs can be regarded as interleaved buck converters, for which the characterization of current ripple under inductance mismatches has been proposed in [13]. This section briefly introduces the analytical method and some results in [13].

The total current ripple is characterized by the peak values and the instant when these peaks occur. As proposed in [13], the normalized peak values $P_x^{\pm}$ can be calculated

$$P^{+}_{x(D)} = \sum_{k=0}^{N-1} A_{x-k} f_k^{+} = \sum_{k=0}^{N-1} A_{x-k}\left[1 - \frac{2k}{N(1-D)}\right] + \sum_{k>N(1-D)}^{N-1} A_{x-k}\left[\frac{2k}{ND(1-D)} - \frac{2}{D}\right] \quad (1)$$

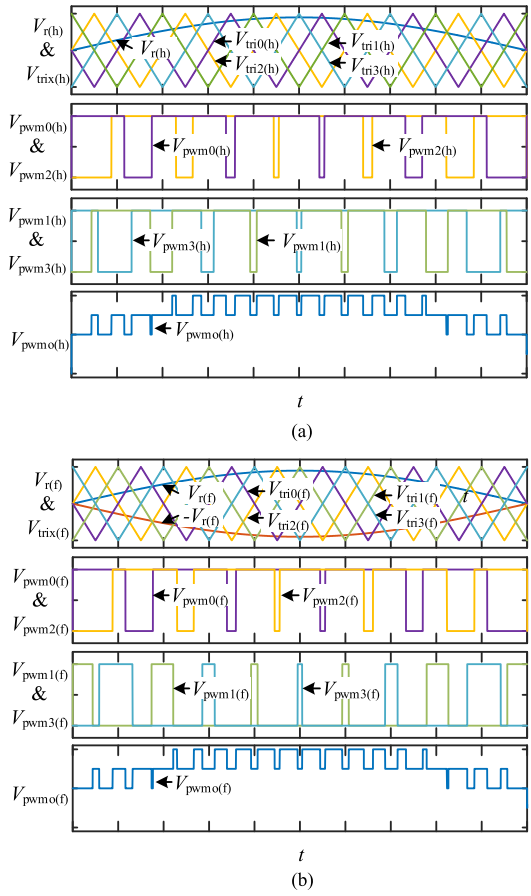

Fig. 4. Illustration of the modulation principle of (a) MHB CDAs and (b) MFB CDAs with four legs.

$$P^{-}_{x(D)} = \sum_{k=0}^{N-1} A_{x-k} f_k^{-} = -\sum_{k=0}^{N-1} A_{x-k}\left[1 - \frac{2k}{ND}\right] - \sum_{k>ND}^{N-1} A_{x-k}\left[\frac{2k}{ND(1-D)} - \frac{2}{1-D}\right] \quad (2)$$

where P_x^{+} (P_x^{-}) is the normalized peak value of the total current ripple when a positive (negative) peak of the phase current ripple in leg x appears. D is the duty ratio. A_x and f(t) define the current ripple of leg x, as shown in (3), where L_x and L_{nom} are the actual and nominal inductances of leg x, respectively. f(t) is a triangular-shaped function of period T, and f_k^{+} (f_k^{-}) is the sample of f(t) at the moment when the positive (negative) current ripple peak of the phase k occur. The time instants corresponding to P_x^{+} and P_x^{-} can also be calculated analytically, as given in

$$r_x(t) = A_x f(t) = \frac{L_{\text{nom}}}{L_x} f(t) \quad (3)$$

$$\begin{cases} t_x^{+} = xT/N \\ t_x^{-} = xT/N - DT. \end{cases} \quad (4)$$

C. Characterization of Current Ripple in MFB CDAs

To overcome this problem, the proposed analytical method tries to find the relationship between $i_{x(f)\,\text{rip}}$ and $i_{k(h)\text{rip}}$. Here,

$i_{k(\mathrm{h})\mathrm{rip}}$ ($k = 0, 1, \ldots, N-1$) is the ripple component of $i_{k(\mathrm{h})}$ in MHB CDAs. According to the modulation principle introduced in Section II-A, the switch action of the same leg between MHB and MFB CDAs happens simultaneously with the same reference signal. Therefore, both $i_{x(\mathrm{f})\mathrm{rip}}$ and $i_{k(\mathrm{h})\mathrm{rip}}$ change linearly during two adjacent switching instants of all the phases. In other words, both $di_{x(\mathrm{f})\mathrm{rip}}/dt$ and $di_{k(\mathrm{h})\mathrm{rip}}/dt$ keep constant and thus $i_{x(\mathrm{f})\mathrm{rip}}$ can be denoted by a linear combination of $i_{x(\mathrm{h})\mathrm{rip}}$ during two adjacent switching instants, as given by

$$i_{x(f)\mathrm{rip}} = \sum_{k=0}^{N-1} \alpha_{xk} i_{k(\mathrm{h})\mathrm{rip}} \tag{5}$$

where α_{xk} is a constant. Then, general analysis is made to prove the existence of α_{xk}, which makes (5) satisfied during the whole switching period *T*. To carry out this analysis, assumptions [13] are made as follows:

1) the analysis is conducted for steady-state operation;
2) the duty ratio *D* is the same for all phases during one switching cycle;
3) the phase current changes linearly between two adjacent switching instants, and therefore can be regarded as the linear segments;
4) the phase shift errors among phases are small compared to the switching period and can be neglected.

Also, the correlation of some parameters between MHB and MFB CDAs needs to be clarified to connect $i_{x(\mathrm{f})\mathrm{rip}}$ with $i_{x(\mathrm{h})\mathrm{rip}}$.

1) The dc bus voltage of MHB CDAs is two times that of MFB CDAs, namely $V_{\mathrm{bus+}} = V_s/2$, $V_{\mathrm{bus-}} = -V_s/2$, and $V_{\mathrm{bus}} = V_s/2$.
2) The phase inductors should have the same ratio, that is, $L_{k(\mathrm{h})}/L_{k(\mathrm{f})} = m$, $k = 0, 1, \ldots, N-1$. Further, if all the phase inductances of MHB CDAs equal to the nominal inductance $L_{\mathrm{nom(h)}}$, the equivalent output inductance is $L_{\mathrm{nom(h)}}/N$. For MFB CDAs, this equivalent output inductance is $4L_{\mathrm{nom(f)}}/N$. Thus, to have the same equivalent inductance, *m* is selected as 4.

Based on the above assumptions and the correlations of the parameters, the parameter α_{xk} can be derived as follows. The detailed derivation is given in the Appendix

$$\alpha_{xk} = \begin{cases} -2L_{\mathrm{eq}}/L_{x(\mathrm{f})}, & k = 0, 2, 4, \ldots, N-2 \text{ and } x \neq k \\ 2\left(1 - L_{\mathrm{eq}}/L_{x(\mathrm{f})}\right), & k = 0, 2, 4, \ldots, N-2 \text{ and } x = k \\ 2L_{\mathrm{eq}}/L_{x(\mathrm{f})}, & k = 1, 3, 5, \ldots, N-1 \text{ and } x \neq k \\ -2\left(1 - L_{\mathrm{eq}}/L_{x(\mathrm{f})}\right), & k = 1, 3, 5, \ldots, N-1 \text{ and } x = k \end{cases} \tag{6}$$

where L_{eq} is the parallel equivalent inductances of all the phase inductors.

$$L_{\mathrm{eq}} = \frac{1}{1/L_{0(\mathrm{f})} + 1/L_{1(\mathrm{f})} + \cdots + 1/L_{(N-1)(\mathrm{f})}}. \tag{7}$$

Therefore, the total current ripple of MFB CDAs is

$$i_{\mathrm{tot(f)rip}} = \sum_{j=0}^{N/2-1} i_{(2j)(\mathrm{f})\mathrm{rip}} = \sum_{k=0}^{N-1} \left(\sum_{j=0}^{N/2-1} \alpha_{(2j)k} \right) i_{k(\mathrm{h})\mathrm{rip}}. \tag{8}$$

Substituting $i_{k(\mathrm{h})\mathrm{rip}}$ with (3), the total current ripple of MFB CDAs can be rewritten as

$$i_{\mathrm{tot(f)rip}} = \sum_{k=0}^{N-1} A'_k f(t) \tag{9}$$

where A'_k is

$$A'_k = A_k \sum_{j=0}^{N/2-1} \alpha_{(2j)k} = \frac{L_{\mathrm{nom(f)}}}{L_{k(\mathrm{f})}} \sum_{j=0}^{N/2-1} \alpha_{(2j)k} \tag{10}$$

where $L_{\mathrm{nom(f)}}$ and $L_{k(\mathrm{f})}$ are the nominal and actual inductances of phase *k* in MFB CDAs. Replacing A_k in (1) and (2) with A'_k, the normalized expression of the positive and negative peaks of total current ripple $i_{\mathrm{tot(f)rip}}$ is presented by the following equations, and the time instants are the same as (4):

$$P^+_{xf(D)} = \sum_{k=0}^{N-1} A'_{x-k} f^+_k = \sum_{k=0}^{N-1} A'_{x-k} \left[1 - \frac{2k}{N(1-D)} \right] + \sum_{k > N(1-D)}^{N-1} A'_{x-k} \left[\frac{2k}{ND(1-D)} - \frac{2}{D} \right] \tag{11}$$

$$P^-_{xf(D)} = \sum_{k=0}^{N-1} A'_{x-k} f^-_k = -\sum_{k=0}^{N-1} A'_{x-k} \left[1 - \frac{2k}{ND} \right] - \sum_{k > ND}^{N-1} A'_{x-k} \left[\frac{2k}{ND(1-D)} - \frac{2}{1-D} \right]. \tag{12}$$

To calculate the total ripple from its normalized value, the results in (11) and (12) should be multiplied by I_{nom}. When $V_{\mathrm{bus}} = V_s/2$, I_{nom} is

$$I_{\mathrm{nom}} = \frac{V_s(1-D)DT}{2L_{\mathrm{nom(h)}}} = \frac{V_s(1-D)DT}{8L_{\mathrm{nom(f)}}}. \tag{13}$$

D. Harmonic Analysis of the Total Current Ripple

Inductance mismatches have a major impact on the harmonic contents of the total current ripple, which can be calculated using the peak values and time instants of the total current ripple. For MFB CDAs, $i_{\mathrm{tot(f)rip}}$ can be denoted by a Fourier series, as given in the following equation:

$$i_{\mathrm{tot(f)rip}}(t) = \sum_{m=1}^{\infty} \left[h_m \cos\left(m\omega t + \varphi_m \right) \right] \tag{14}$$

where $h_m = \sqrt{a_m^2 + b_m^2}$ and a_m and b_m can be calculated as

$$\begin{cases} a_m = \frac{2}{T} \int_0^T i_{\mathrm{tot(f)rip}}(t) \cos m\omega t \, dt \\ b_m = \frac{2}{T} \int_0^T i_{\mathrm{tot(f)rip}}(t) \sin m\omega t \, dt. \end{cases} \tag{15}$$

As shown in Section II-C, $i_{\mathrm{tot(f)rip}}$ can be denoted piecewise linearly, as

$$r_j(t) = \frac{P_{j+1} - P_j}{t_{j+1} - t_j}(t - t_j) + P_j, \quad t_j < t < t_{j+1}. \tag{16}$$

Therefore, the integration in (15) can also be calculated by segments. The final results of a_m and b_m are presented by the

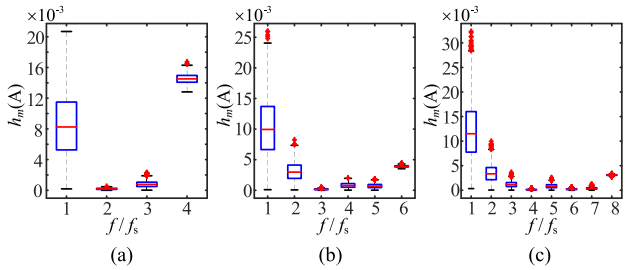

Fig. 5. Boxplots of the harmonic contents of the total current ripple. (a) $N = 4$. (b) $N = 6$. (c) $N = 8$.

following equation, which can be used to study the impact of inductance mismatches on the harmonic contents of the total current ripple:

$$\begin{cases} a_m = \frac{1}{m\pi} \sum_{j=0}^{2N-1} \left[\begin{array}{l} P_{j+1} \sin(m\omega t_{j+1}) - P_j \sin(m\omega t_j) \\ + \frac{P_{j+1}-P_j}{t_{j+1}-t_j} \frac{\cos(m\omega t_{j+1}) - \cos(m\omega t_j)}{m\omega} \end{array} \right] \\ b_m = \frac{1}{m\pi} \sum_{j=0}^{2N-1} \left[\begin{array}{l} P_j \cos(m\omega t_j) - P_{j+1} \cos(m\omega t_{j+1}) \\ + \frac{P_{j+1}-P_j}{t_{j+1}-t_j} \frac{\sin(m\omega t_{j+1}) - \sin(m\omega t_j)}{m\omega} \end{array} \right] \end{cases}. \tag{17}$$

III. Worst Case Analysis

The inductance mismatches impact the harmonic contents of the current ripple, which further influences the output total harmonic distortion (THD) under the sinusoidal signal modulation. The worst case analysis is necessary for designers to evaluate the system performance under the inductance mismatches. Monte Carlo simulation is used in [6] to identify the worst case when the demanding output filter capacitance is maximum. The same method is used here to study the effects of inductance mismatches on the harmonic contents of the total current ripple for MFB CDAs. The harmonic contents taken into consideration are the harmonic of kf_s $(k = 1, 2, \ldots, N)$. As shown in Section II-C, to calculate the normalized total current ripple, only normalized inductances are needed. Therefore, the normalized phase inductances are chosen as variables, which are generated randomly within predefined tolerance e_{tol}. The analysis is conducted under the sinusoidal signal modulation. The modulation frequency $f_0 = 1$ kHz and the switching frequency $f_s = 100$ kHz.

To conduct Monte Carlo simulations, the inductance tolerance e_{tol}, phase number *N,* and modulation ratio *M* are defined first. Besides, V_s and $L_{\text{nom(f)}}$ should also be given to calculate the nominal ripple current I_{nom}. Then, the duty ratio *D* is calculated according to the modulation signal, which is sampled at each switching cycle *T*. With duty ratio *D* and generated random phase inductances, the total current ripple is calculated. Finally, the harmonic contents can be calculated using (17). Fig. 5 shows the analytical results when the inductance tolerance is 15%, and the phase number is 4, 6, and 8, respectively. The number of samples is 2000. The other parameters are defined as $M = 0.9$, $V_s = 400$ V, and $L_{\text{nom(f)}} = 190\,\mu$H.

The boxplot is a useful tool to display the distribution of data [17]. The central rectangle in the boxplot spans the first quartile to the third quartile, denoted by *IQR* (the interquartile range), which reflects the likely range of variation. As shown in Fig. 5, the inductance mismatches mainly affect the harmonic content at f_s. Therefore, the worst case refers to the case when the harmonic content at f_s is maximum. The normalized phase inductance values $L_{x\text{(f)nom}}$ in the worst case is listed in Table I.

TABLE I
Normalized Phase Inductance Values in the Worst Case

	$N = 4$	$N = 6$	$N = 8$
$L_{0\text{(f)nom}}$	1.15	1.11	1.13
$L_{2\text{(f)nom}}$	0.86	1.03	0.91
$L_{4\text{(f)nom}}$	—	0.86	0.85
$L_{6\text{(f)nom}}$	—	—	1.11
$L_{1\text{(f)nom}}$	0.86	1.13	1.05
$L_{3\text{(f)nom}}$	1.09	0.85	0.90
$L_{5\text{(f)nom}}$	—	1.04	0.90
$L_{7\text{(f)nom}}$	—	—	1.12

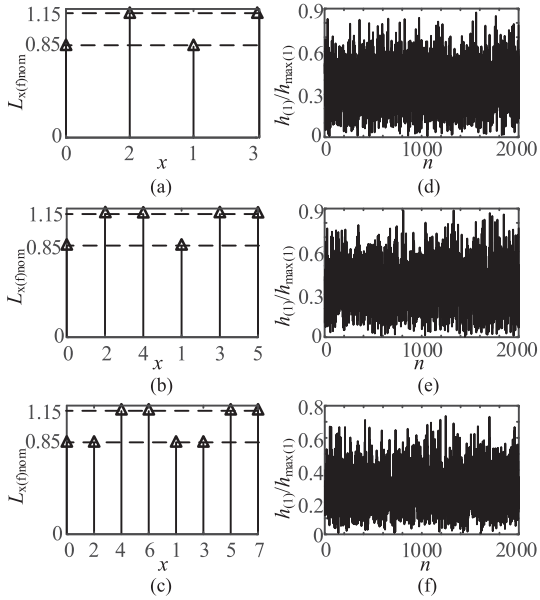

Fig. 6. Comparison of the harmonic content at f_s of the total current ripple. (a) $N = 4$. (b) $N = 6$. (c) $N = 8$. (d) $N = 4$. (e) $N = 6$. (f) $N = 8$.

As indicated in Table I, the worst case occurs when the phase inductors in the upper (lower) phase group are equally or nearly equally distributed above and below the nominal phase inductance. Here, the upper phase group refers to the phases with phase number $k = 0, 2, \ldots, N-2$, and the lower phase group refers to the phases with phase number $k = 1, 3, \ldots, N-1$, as shown in Fig. 1(b). Therefore, considering the whole range of the phase inductances, the worst case happens when the imbalance of the phase inductances in the upper or lower phase is maximum, which means the phase inductances are equally distributed to their maximum and minimum limits, as shown in Fig. 6(a)–(c). For further verification, Fig. 6(d)–(f) compares the harmonic content at f_s of the total current ripple between the Monte Carlo simulation results and the calculated value when the phase inductances are distributed as in Fig. 6(a)–(c). Here, $h_{(1)}$ stands for the harmonic content at f_s under the inductances

TABLE II
HARMONIC CONTENTS WITH DIFFERENT DISTRIBUTION OF INDUCTANCES UNDER THE WORST CASE

	Distribution of phase inductances, $[L_{0(f)nom}, L_{2(f)nom}, L_{1(f)nom}, L_{3(f)nom}]$	The harmonic content at f_s, $h_{max(1)}$ (A)
Case 1	[0.85, 1.15, 0.85, 1.15]	0.02378
Case 2	[1.15, 0.85, 0.85, 1.15]	0.02329
Case 3	[0.85, 1.15, 1.15, 0.85]	0.02292
Case 4	[1.15, 0.85, 1.15, 0.85]	0.02371

TABLE III
SIMULATION PARAMETERS FOR THE FOUR-LEG MHB AND MFB CDA

Simulation	**MFB CDA**		**MHB CDA**	
Description	**Variable**	**Value**	**Variable**	**Value**
DC bus voltage	V_{bus} (V)	200	V_{bus+} (V)	200
			V_{bus-} (V)	-200
Switching period	T (μs)	10	T (μs)	10
Modulation period	T_0 (ms)	1	T_0 (ms)	1
Modulation ratio	M	0.9	M	0.9
Output Capacitor	C_f(nF)	180	C_f(nF)	180
Load Resistor	R_{load} (Ω)	30	R_{load} (Ω)	30
Nominal phase inductance	$L_{n(f)}$ (μH)	190	$L_{n(f)}$ (μH)	760
Phase inductance	$L_{0(f)}$ (μH)	219.4	$L_{0(h)}$ (μH)	877.6
	$L_{2(f)}$ (μH)	163.4	$L_{2(h)}$ (μH)	653.6
	$L_{1(f)}$ (μH)	163.1	$L_{1(h)}$ (μH)	652.4
	$L_{3(f)}$ (μH)	217.9	$L_{3(h)}$ (μH)	871.6

of sample n, and $h_{max(1)}$ is the harmonic content at f_s when the inductances are distributed as shown in Fig. 6(a)–(c). The ratio $h_{(1)}/h_{max(1)}$ is always smaller than 1 in Fig. 6(d)–(f), which verifies that Fig. 6(a)–(c) refers to the distribution of inductances in the worst case.

Also, the influence of different permutation of phase inductances on the harmonics of the total current ripple in the worst case is analyzed. The analytical results for $N = 4$ is shown in Table II. The maximum deviation of $h_{max(1)}$ among the four cases is 3.62%, which reveals that in the worst case, the different permutation of phase inductances in the upper or lower phase group has insignificant impact on the harmonic content at f_s in the total current ripple.

IV. SIMULATION AND EXPERIMENTAL VERIFICATION

The four-leg MHB and MFB CDAs are simulated in the Simulink. The simulation parameters of the MFB CDAs are given according to the experimental prototype, as introduced later. While the simulation parameters of the MHB CDAs are given according to the conversion rules introduced in Section II-C. The detailed simulation parameters are given in Table III.

Fig. 7 shows the simulated and analytical waveforms of inductor current ripple $i_{x(f)rip}$. The analytical $i_{x(f)rip}$ is calculated using (5), where the $i_{k(h)rip}$ is the simulated inductor current ripple from the MHB CDA simulation. The simulated $i_{x(f)rip}$ and $i_{k(h)rip}$ are extracted from the simulated $i_{x(f)}$ and $i_{k(h)}$, as follows:

$$\begin{cases} i_{x(f)rip} = i_{x(f)} - i_{x(f)sig} \\ i_{k(h)rip} = i_{k(h)} - i_{k(h)sig} \end{cases} \tag{18}$$

where $i_{x(f)sig}$ and $i_{k(h)sig}$ are the low-frequency signal component of $i_{x(f)}$ and $i_{k(h)}$, respectively.

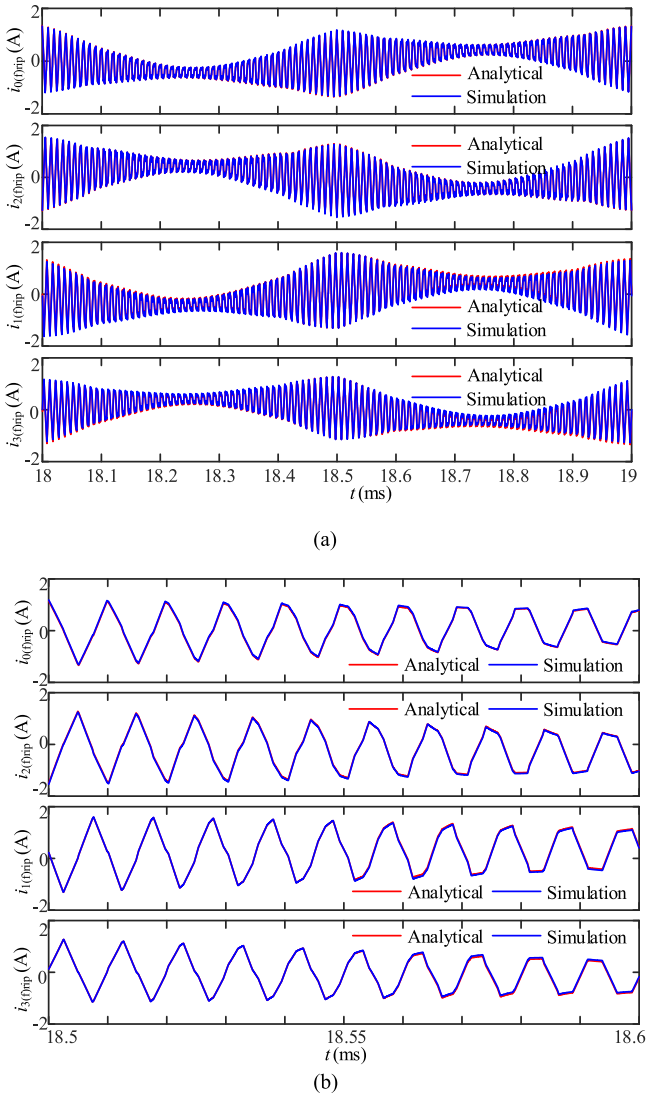

Fig. 7. Comparison between simulated and analytical $i_{x(f)rip}$. (a) Waveforms of $i_{x(f)rip}$ in one modulation period T_0. (b) Waveforms of $i_{x(f)rip}$ during small time interval as $T_0/10$.

For simplicity, the $i_{x(f)sig}$ and $i_{k(h)sig}$ are estimated as follows:

$$i_{x(f)sig} = \begin{cases} 2i_o/N, & \text{when } x = 0, 2, 4, \ldots, N-2 \\ -2i_o/N, & \text{when } x = 1, 3, 5, \ldots, N-1 \end{cases} \tag{19}$$

$$i_{k(h)sig} = i_o/N \tag{20}$$

where i_o is the load current, and N is the number of legs.

As shown in Fig. 7, the simulated and analytical waveforms of $i_{x(f)}$ coincide well, which verifies the relationship between MHB and MFB CDAs, as given in (5).

To verify the proposed analytical method, a four-leg MFB CDA experimental prototype was built, as shown in Fig. 8. The PSCM was realized in the field programmable gate array (XC6SLX16 from Xilinx) using the triangular carriers. The semiconductor devices used in the prototype are SiC MOSFETs (C2M0080120D from Wolfspeed) [18] and SiC Schottky Barrier Diodes (C4D30120D from Wolfspeed) [19]. The other parameters are the same as listed in Table III for the MFB CDA.

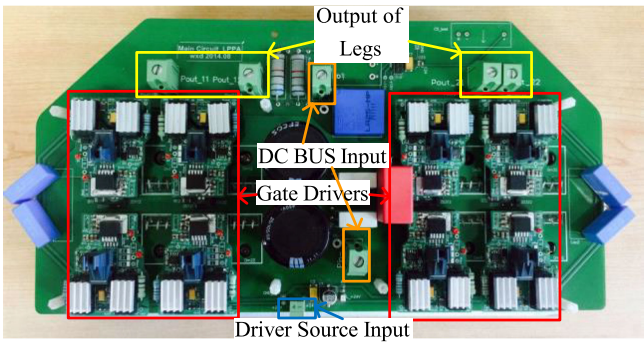

Fig. 8. Four-leg MFB CDA prototype.

The phase inductors are built with the double-C gapped amorphous cores and Litz wire winding, with a ±15% inductance tolerance: $L_{0(f)} = 219.4\,\mu$H, $L_{2(f)} = 163.4\,\mu$H, $L_{1(f)} = 163.1\,\mu$H, and $L_{3(f)} = 217.9\,\mu$H. The inductance values correspond to the inductance values in the worst case for $N = 4$, referred as case 1. For comparisons, the permutation of the phase inductance values changes to: $L_{0(f)} = 219.4\,\mu$H, $L_{2(f)} = 217.9\,\mu$H, $L_{1(f)} = 163.1\,\mu$H, and $L_{3(f)} = 163.4\,\mu$H, referred as case 2. The tolerances lead to the difference among the amplitude of the phase current ripples, reflected by $A_k^{'}$ in (9), yielding $A_0^{'} = 0.868$, $A_1^{'} = 1.163$, $A_2^{'} = 1.165$, and $A_3^{'} = 0.870$ in case 1 and $A_0^{'} = 0.992$, $A_1^{'} = 0.996$, $A_2^{'} = 0.998$, and $A_3^{'} = 0.994$ in case 2. This also indicates that the imbalance among the phase current ripples is mainly caused by the inductance mismatches in the same leg group of MFB CDA. As for case 2, although the tolerance of all the phase inductors is still ±15%, the phase inductance values in the upper (lower) group are consistent, leading to a slight difference among the amplitude of the phase current ripples. Therefore, case 2 can be approximated as the ideal case.

Fig. 9 compares the analytical total current ripple $i_{\text{rip(f)}}$ and the simulated $i_{L\,\text{sum(f)}}$ under different duty ratio D. Regardless of the low-frequency signal component of $i_{L\,\text{sum(f)}}$, the analytical $i_{\text{rip(f)}}$ characterize the current ripple of $i_{L\,\text{sum(f)}}$ with good accuracy, which is further verified by comparing the analytical $i_{\text{rip(f)}}$ with the experimental waveforms of $i_{L\,\text{sum(f)}}$. The high-frequency ringing present in the experimental waveforms is caused by the switching device and the converter parasitic elements [20].

Fig. 10 shows the harmonics of experimental waveform and the calculated harmonics using (17), which are relatively consistent. The amplitude errors are caused by the noises in the experimental and measurement setup. As indicated in Fig. 10, when comparing case 1 with case 2, the harmonic content of the total current ripple at $4f_s$ is almost the same under the same duty ratio D, while the harmonic content at f_s in case 1 is much larger than that in case 2. Therefore, with inductance mismatches in the upper or lower leg group of MFB CDAs, the harmonic content of the total current ripple at switching frequency and its harmonics are no longer canceled, which influences the quality of the output waveform. This is verified by Fig. 11, which presents the experimental waveform of the output voltage v_o and the total output current $i_{L\,\text{sum(f)}}$ under 1 kHz sinusoidal modulation in case 1 and 2. Due to the degradation of ripple cancelation effects, the THD of $i_{L\,\text{sum(f)}}$ is 7.28% in case 1, which is about 1.6 times of that in case 2. As for the output voltage, the THD of v_o is 3.85% in case 1, slightly higher than that in case 2 (3.55%). Taking currents for example, the calculation of THD is based on the equation given as follows:

$$\text{THD} = \sqrt{I_2^2 + I_3^2 + \cdots + I_n^2}/I_1 \tag{21}$$

where I_1 is the rms value of the fundamental current, and I_n is the rms value of the harmonic n. The maximum frequency is selected as $4f_s$, namely 400 kHz.

It should be noted that the cutoff frequency of the output filter is 27.2 kHz based on the parameters given in Table II. Therefore, the harmonic contents of $i_{L\,\text{sum(f)}}$ at switching frequency and its harmonics are mostly filtered out, leading to a slight difference in the THD of v_o between case 1 and 2. However, if the filter is designed based on the equivalent switching frequency Nf_s, the cutoff frequency can be set even close to the switching frequency to reduce the size of the filter. On this occasion, the harmonic contents of $i_{L\,\text{sum(f)}}$ at the switching frequency and its low order harmonics are only partly filtered out, rendering severe impact on the THD of v_o under inductance mismatches. In other words, the phase inductance mismatches make it more difficult to deal with the tradeoff between low THD and size reduction of the output filter.

V. Design Guideline

The proposed analytical method can act as an effective analytical tool to optimize the design of the output filter considering the inductance mismatches. To design the parameters of the output filter, the nominal phase inductance is first considered. The nominal phase inductance $L_{\text{nom(f)}}$ is related to the maximum allowable output current ripple, as given by (22), where σ_i is the maximum allowable ratio of the output current ripple to the steady-state load current I_o. Then, the output capacitance is selected according to the cutoff frequency f_c of the output filter. For *N*-leg MFB CDAs, f_c is selected between the maximum modulation frequency f_0 and the equivalent switching frequency Nf_s. Then, the output capacitor C_f is given as follows:

$$L_{\text{nom(f)}} \geq V_{\text{bus}}/\left(16Nf_s\sigma_i I_o\right) \tag{22}$$

$$C_f = N/\left(16\pi^2 f_c^2 L_{\text{nom(f)}}\right). \tag{23}$$

While the specific value of f_c can be obtained by the given attenuation level of the high-frequency contents of the output voltage, namely the harmonic contents at and above the switching frequency f_s. The harmonic content at kf_s of the output voltage can be calculated as $h_k R_{\text{load}} \alpha_v(kf_s)$, where h_k is the harmonic content at kf_s of the total current ripple, and $\alpha_v(\text{f})$ can be obtained as (24), according to the amplitude-frequency response of the output filter

$$\alpha_v(f) = 1/\sqrt{1 + \frac{N^2 f^2 R_{\text{load}}^2}{64\pi^2 f_c^4 L_{\text{nom(f)}}^2}}. \tag{24}$$

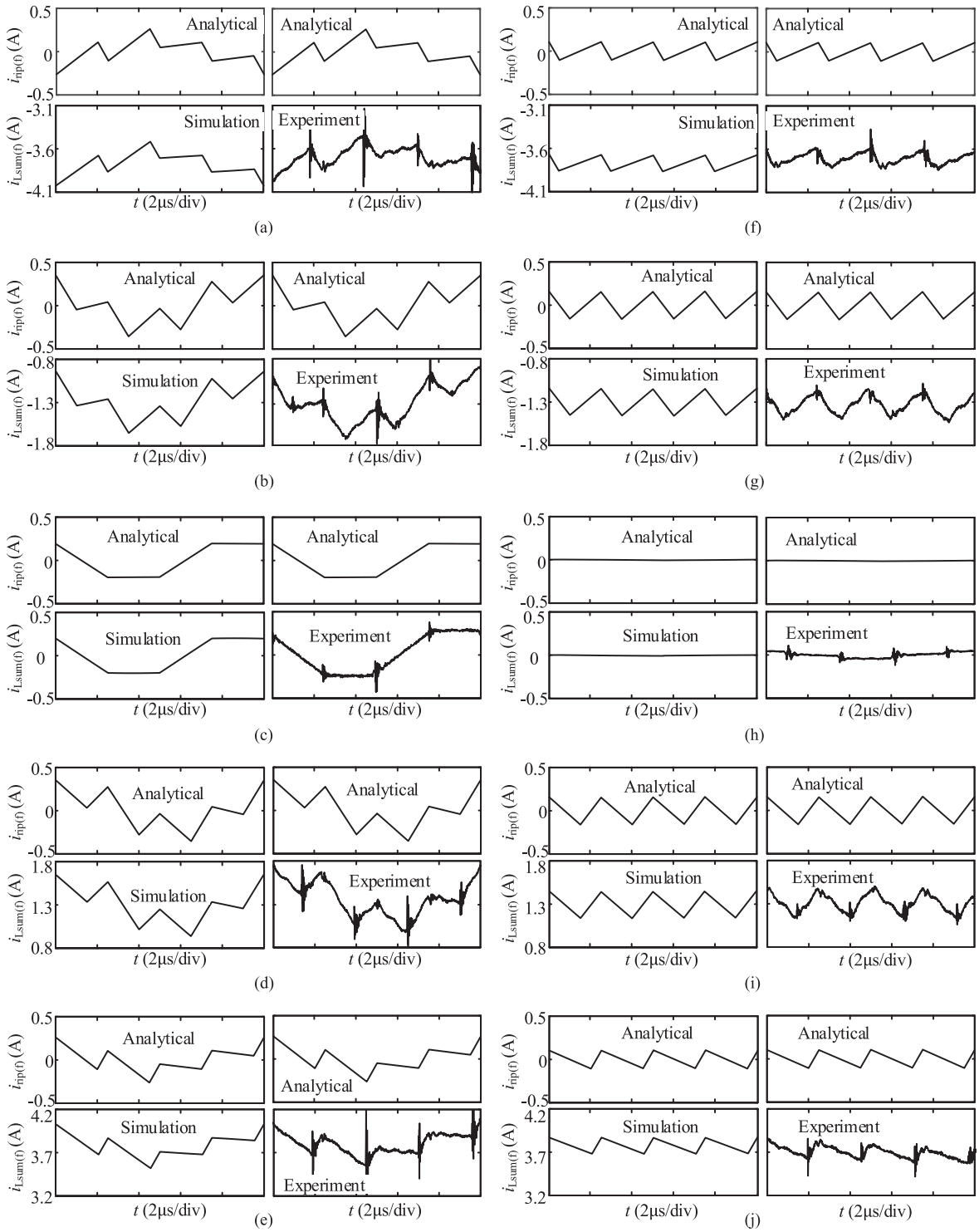

Fig. 9. Analytical, simulated, and experimental total current ripple under different *D*. [(a) ∼ (e) for case 1; (f) ∼ (j) for case 2]. (a) Case1, $D = 0.2$. (b) Case1, $D = 0.4$. (c) Case1, $D = 0.5$. (*D*) Case1, $D = 0.6$. (e) Case1, $D = 0.8$. (f) Case2, $D = 0.2$. (g) Case2, $D = 0.4$. (h) Case2, $D = 0.5$. (i) Case2, $D = 0.6$. (j) Case2, $D = 0.8$.

Therefore, the selection of f_c should satisfy $h_k R_{\text{load}}$ $\alpha_v(kf_s) \leq h_{v\text{lim}}$, where $h_{v\text{lim}}$ is the given maximum level of high-frequency component of the output voltage. When the inductance mismatches are neglected, the high-frequency component dominates at or near Nf_s, denoted by h_N. Then, according to $h_N R_{\text{load}} \alpha_v(Nf_s) \leq h_{v\text{lim}}$, the maximum allowable cutoff frequency is given by

$$f_{c1} = Nf_s \sqrt{\frac{\alpha_{v\text{lim}}(Nf_s) R_{\text{load}}}{8\pi f_s L_{\text{nom(f)}} \sqrt{1 - \alpha_{v\text{lim}}^2(Nf_s)}}} \tag{25}$$

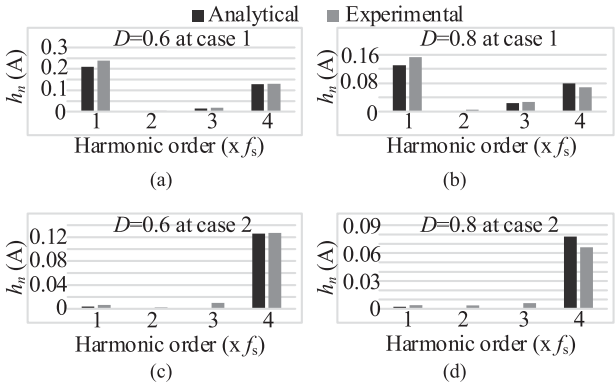

Fig. 10. Analytical and experimental harmonics of total current ripple in case 1 and case 2.

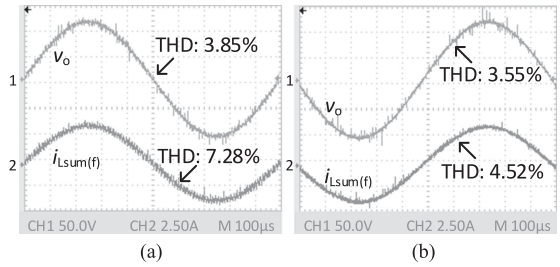

Fig. 11. Output waveform of v_o and $i_{L\,\mathrm{sum(f)}}$ in (a) case 1 and (b) case 2.

where $\alpha_{v\mathrm{lim}}(Nf_s) = h_{v\mathrm{lim}}/(h_N R_{\mathrm{load}})$ is the maximum attenuation factor at Nf_s.

However, with inductance mismatches considered, the high-frequency harmonic content appears at f_s. Therefore, the criterion given by (25) should be modified as (26) to ensure all the high-frequency components of the output voltage are below the limit $h_{v\mathrm{lim}}$. It should be noted that $\alpha_{v\mathrm{lim}}(Nf_s)$ and $\alpha_{v\mathrm{lim}}(f_s)$ should be calculated under the worst case with the given tolerance of the phase inductances e_{tol}, as introduced in Section III

$$f_{c2} = \min\left(\begin{array}{l} Nf_s\sqrt{\dfrac{\alpha_{v\,\mathrm{lim}}(Nf_s)R_{\mathrm{load}}}{8\pi f_s L_{\mathrm{nom(f)}}\sqrt{1-\alpha^2_{v\,\mathrm{lim}}(Nf_s)}}} \\ Nf_s\sqrt{\dfrac{\alpha_{v\,\mathrm{lim}}(f_s)R_{\mathrm{load}}}{8\pi Nf_s L_{\mathrm{nom(f)}}\sqrt{1-\alpha^2_{v\,\mathrm{lim}}(f_s)}}} \end{array}\right). \quad (26)$$

The simulation of a four-leg MFB CDA is conducted to verify the impact of inductance mismatches on the output capacitor or the cutoff frequency. The simulation parameters are the same as listed in Table III. Fig. 12 shows the calculated harmonic contents of the total current ripple under the ideal case and the worst case when the inductance tolerance e_{tol} is 15%, which reveals that $h_1 = 0.062$ A, and $h_N = 0.036$ A. Therefore, under the same $h_{v\mathrm{lim}}$, the relationship between $\alpha_{v\mathrm{lim}}(Nf_s)$ and $\alpha_{v\mathrm{lim}}(f_s)$ is obtained as

$$\alpha_{v\mathrm{lim}}(f_s)/\alpha_{v\mathrm{lim}}(Nf_s) = h_N/h_1 = 0.5645. \quad (27)$$

The attenuation factor $\alpha_{v\mathrm{lim}}(Nf_s)$ is given as 0.1 for example. Then, f_{c1} is calculated as 31.8 kHz and f_{c2} is calculated as 11.9 kHz. Fig. 13 compares the simulation results of the

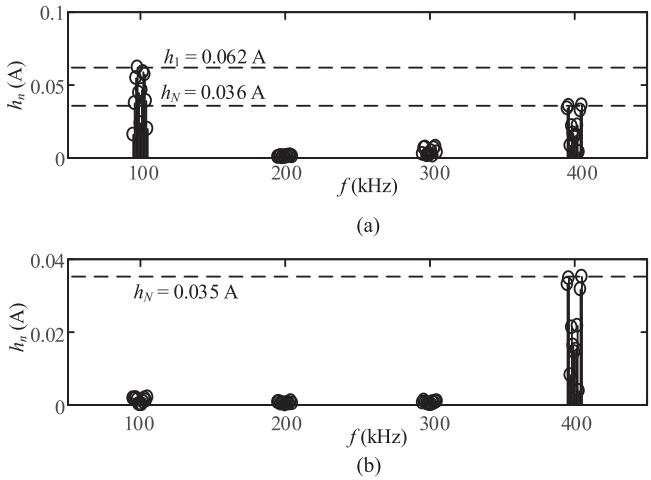

Fig. 12. Calculated high-frequency harmonic contents of the total current ripple. (a) Worst case. (b) Ideal case.

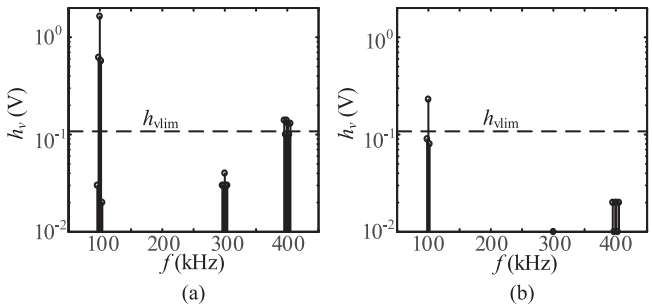

Fig. 13. Simulation results of the high-frequency harmonic contents of the output voltage. (a) $f_c = f_{c1}$. (b) $f_c = f_{c2}$.

high-frequency harmonic contents of the output voltage when the cutoff frequency is f_{c1} and f_{c2}, respectively. As shown in Fig. 13, when f_c is calculated without considering the inductance mismatches ($f_c = f_{c1}$), the harmonic content near f_s (100 kHz) exceeds the maximum limit $h_{v\mathrm{lim}}$ by more than an order of magnitude. While when f_c is calculated by considering the inductance mismatches ($f_c = f_{c2}$), the harmonic contents of the output voltage are all below or near $h_{v\mathrm{lim}}$, which shows the effectiveness of the proposed design strategy of the output filter by considering the phase inductance mismatches. Also, (26) can be used to select the maximum allowable tolerance of the phase inductance, when the cutoff frequency f_c is given, which is helpful for the designers to design or select inductors.

VI. Conclusion

The main benefit of multileg CDAs under the PSCM is the increase of effective switching frequency, leading to higher bandwidth. This benefit, however, can be degenerated by the mismatch of phase inductances, which can be attributed to the tolerances in the manufacturing process and the magnetic materials. This mismatch of phase inductances results in the imbalance of the amplitude of the phase current ripples, which generates the switching frequency component and its harmonics

in the total current ripple, and thus influences the quality of the output waveform.

This paper proposes a general analytical method to calculate the total current ripple in MFB CDAs considering inductance mismatches. The proposed method utilizes the relationship of the phase current ripple between MFB and MHB CDAs to avoid the difficulty and complexity of characterizing the phase current ripple in MFB CDAs directly. Using the proposed method, the influence of inductance mismatches on the harmonic contents of the total current ripple is investigated. Monte Carlo simulation is conducted to identify the phase inductance values and distribution in the worst case. Then, it is convenient for the designers to directly evaluate the performance of the MFB CDAs in the worst case. Such evaluation is helpful for the designers to design the parameters of the output filter and select the allowed maximum tolerances of the phase inductances. Finally, the proposed analytical method is verified by simulation and experimental results. Also, the proposed analytical method can be applied to multileg inverters with the same topology as MFB CDAs.

APPENDIX

This section introduces the derivation of (6). $S_{k(\mathrm{h})}(t)$ and $S_{k(\mathrm{f})}(t)$ are the switching function of leg *k* in MHB and MFB CDAs, respectively. For MHB CDAs, $S_{k(\mathrm{h})}(t)=1$ means the output voltage of leg *k* is $V_{\mathrm{bus+}}$ (V_s/2), and $S_{k(\mathrm{h})}(t)=0$ means the output voltage of leg *k* is $V_{\mathrm{bus-}}$ ($-V_s$/2). For MFB CDAs, $S_{k(\mathrm{f})}(t)=1$ means the output voltage of leg *k* is V_{bus} (V_s/2), and $S_{k(\mathrm{f})}(t)=0$ means the output voltage of leg *k* is 0.

According to the modulation principle, the switching actions of leg *k* in MHB and MFB CDAs occur at the same time under the same reference signal. Here, t_m is the time instant when $S_{k(\mathrm{h})}$ changes from 0 to 1. t_{m-1} and t_{m+1} are the time instants when the closest switching action of all the phases happens before and after t_m. Considering the other legs except leg *k* during the time interval $t_{m-1}<t<t_{m+1}$, *p* and *N*–1–*p* (*q* and *N*–1–*q*) are defined as the number of legs of MHB CDAs (MFB CDAs) whose switching function stays at 0 and 1, respectively.

A. When $k=2j$ ($j=0,1,\ldots,N/2-1$): According to the modulation principle shown in Fig. 2, $S_{k(\mathrm{f})}$ changes from 0 to 1 at time t_m. Here, we define S_{LH} and S_{RH} as the left-hand and right-hand side of (5), respectively.

At time interval $t_{m-1}<t<t_m$, $S_{k(\mathrm{h})}(t)=0$, $S_{k(\mathrm{f})}(t)=0$. Therefore, the derivative of S_{LH} at this time interval can be denoted by

$$\frac{dS_{\mathrm{LH}}}{dt}=\frac{\frac{V_s}{2}\lambda_1(x,t)+(v_b-v_a)\lambda_2(x)-v_b}{L_{x(\mathrm{f})}} \tag{28}$$

where

$$\lambda_1(x,t)=\begin{cases}1, & \text{when } S_{x(\mathrm{f})}(t)=1\\ 0, & \text{when } S_{x(\mathrm{f})}(t)=0\end{cases} \tag{29}$$

$$\lambda_2(x)=\begin{cases}1, & \text{when } x=2j(j=0,1,\ldots,N/2-1)\\ 0, & \text{when } x=2j+1(j=0,1,\ldots,N/2-1).\end{cases} \tag{30}$$

With the positive direction defined in Fig. 1, the sum of all the phase currents of MFB CDAs equals to 0

$$\sum_{j=0}^{N-1} i_{j(\mathrm{f})}=0. \tag{31}$$

The derivative of (31) yields

$$\sum_{j=0}^{N/2-1}\left(\frac{1}{L_{(2j)(\mathrm{f})}}\right)v_a+\sum_{j=0}^{N/2-1}\left(\frac{1}{L_{(2j+1)(\mathrm{f})}}\right)v_b=\sum_{j=1}^{N-q-1}\left(\frac{1}{L_{q_j(\mathrm{f})}}\right)\frac{V_s}{2} \tag{32}$$

where $L_{q_j(\mathrm{f})}$ is the phase inductor of the phases whose switching function equals to 1 at time interval $t_{m-1}<t<t_m$. Also, v_a and v_b satisfy

$$v_a-v_b=v_o. \tag{33}$$

Based on (28), (32), and (33), the derivative of S_{LH} can be rewritten as

$$\frac{dS_{\mathrm{LH}}}{dt}=\frac{\lambda_1(x,t)V_s}{2L_{x(\mathrm{f})}}+\frac{L_{\mathrm{eq}}}{L_{x(\mathrm{f})}}\left[\frac{(1-\lambda_2(x))\,v_{\mathrm{o}}}{L_{\mathrm{eq1}}}-\frac{\lambda_2(x)v_{\mathrm{o}}}{L_{\mathrm{eq2}}}-\frac{V_s}{2L_{\mathrm{eq3}}}\right] \tag{34}$$

where L_{eq}, L_{eq1}, L_{eq2}, and L_{eq3} are

$$\begin{cases}L_{\mathrm{eq}}=1/\sum_{j=0}^{N-1}\left(1/L_{j(\mathrm{f})}\right)\\ L_{\mathrm{eq1}}=1/\sum_{j=0}^{N/2-1}\left(1/L_{(2j)(\mathrm{f})}\right)\\ L_{\mathrm{eq2}}=1/\sum_{j=0}^{N/2-1}\left(1/L_{(2j+1)(\mathrm{f})}\right)\\ L_{\mathrm{eq3}}=1/\sum_{j=1}^{N-q-1}\left(1/L_{q_j(\mathrm{f})}\right).\end{cases} \tag{35}$$

The derivative of S_{RH} at time interval $t_{m-1}<t<t_m$ is

$$\frac{dS_{\mathrm{RH}}}{dt}=\left(-\frac{V_s}{2}-v_o\right)\left[\sum_{j=1}^{p}\left(\frac{\alpha_{xa_j}}{L_{a_j(\mathrm{h})}}\right)+\frac{\alpha_{xk}}{L_{k(\mathrm{h})}}\right]+\left(\frac{V_s}{2}-v_o\right)\sum_{j=p+2}^{N}\left(\frac{\alpha_{xa_j}}{L_{a_j(\mathrm{h})}}\right) \tag{36}$$

where a_j ($j=1,2,\ldots,p$) is the leg number whose switching function stays at 0, and a_j ($j=p+2,p+3,\ldots,N$) is the leg number whose switching function stays at 1. Substituting (34) and (36) into the differential form of (5), we can obtain

$$\frac{\lambda_1(x,t)V_s}{2L_{x(\mathrm{f})}}+\frac{L_{\mathrm{eq}}}{L_{x(f)}}\left[\frac{(1-\lambda_2(x))\,v_o}{L_{\mathrm{eq1}}}-\frac{\lambda_2(x)v_o}{L_{\mathrm{eq2}}}-\frac{V_s}{2L_{\mathrm{eq3}}}\right]=\left(-\frac{V_s}{2}-v_o\right)\left[\sum_{j=1}^{p}\left(\frac{\alpha_{xa_j}}{L_{a_j(\mathrm{h})}}\right)+\frac{\alpha_{xk}}{L_{k(h)}}\right]+\left(\frac{V_s}{2}-v_o\right)\sum_{j=p+2}^{N}\left(\frac{\alpha_{xa_j}}{L_{a_j(\mathrm{h})}}\right). \tag{37}$$

At time interval $t_m < t < t_{m+1}$, $S_{k(\mathrm{h})}(t) = 1$, $S_{k(\mathrm{f})}(t) = 1$. Therefore, the derivative of S_{LH} and S_{RH} at this time interval can be calculated as

$$\frac{dS_{\mathrm{LH}}}{dt} = \frac{\lambda_1(x,t)V_s}{2L_{x(\mathrm{f})}} + \frac{L_{\mathrm{eq}}}{L_{x(f)}}\left[\frac{[1-\lambda_2(x)]\,v_o}{L_{\mathrm{eq1}}} - \frac{\lambda_2(x)v_o}{L_{\mathrm{eq2}}} - \left(\frac{1}{L_{\mathrm{eq3}}} + \frac{1}{L_{k(\mathrm{f})}}\right)\frac{V_s}{2}\right] \tag{38}$$

$$\frac{dS_{\mathrm{RH}}}{dt} = \left(-\frac{V_s}{2} - v_o\right)\sum_{j=1}^{p}\left(\frac{\alpha_{xa_j}}{L_{a_j(\mathrm{h})}}\right) + \left(\frac{V_s}{2} - v_{\mathrm{o}}\right)\left[\sum_{j=p+2}^{N}\left(\frac{\alpha_{xa_j}}{L_{a_j(\mathrm{h})}}\right) + \frac{\alpha_{xk}}{L_{k(\mathrm{h})}}\right]. \tag{39}$$

Substituting (38) and (39) into the differential form of (5), we can obtain

$$\frac{\lambda_1(x,t)V_s}{2L_{x(\mathrm{f})}} + \frac{L_{\mathrm{eq}}}{L_{x(\mathrm{f})}}\left[\frac{[1-\lambda_2(x)]\,v_o}{L_{\mathrm{eq1}}} - \frac{\lambda_2(x)v_o}{L_{\mathrm{eq2}}} - \left(\frac{1}{L_{\mathrm{eq3}}} + \frac{1}{L_{\mathrm{k(f)}}}\right)\frac{V_s}{2}\right] = \left(-\frac{V_s}{2} - v_o\right)\sum_{j=1}^{p}\left(\frac{\alpha_{xa_j}}{L_{a_j(\mathrm{h})}}\right) + \left(\frac{V_s}{2} - v_o\right)\left[\sum_{j=p+2}^{N}\left(\frac{\alpha_{xa_j}}{L_{a_j(\mathrm{h})}}\right) + \frac{\alpha_{xk}}{L_{k(h)}}\right]. \tag{40}$$

According to (37), (40) and the relationship between the phase inductance of MHB and MFB CDAs, namely $L_{k(\mathrm{h})}/L_{k(\mathrm{f})} = 4$ ($k = 0,1,\ldots,N$- 1), the parameter α_{xk} can be represented by

$$\alpha_{xk} = \begin{cases} -2L_{\mathrm{eq}}/L_{x(\mathrm{f})}, & x \neq k \\ 2\left(1 - L_{\mathrm{eq}}/L_{x(\mathrm{f})}\right), & x = k. \end{cases} \tag{41}$$

B. When $k = 2j + 1$ ($j = 0,1,\ldots,N/2-1$): According to the modulation principle shown in Fig. 2, $S_{k(\mathrm{f})}$ changes from 1 to 0 at time t_m in this case. Following similar analysis in case A, we can derive α_{xk} in this case as

$$\alpha_{xk} = \begin{cases} 2L_{\mathrm{eq}}/L_{x(\mathrm{f})}, & x \neq k \\ -2\left(1 - L_{\mathrm{eq}}/L_{x(\mathrm{f})}\right), & x = k. \end{cases} \tag{42}$$

Therefore, combining (41) and (42) in each case, we can obtain the results given by (6). It should be noted that the results in (6) can make (5) satisfied at the time interval $t_{m-1} < t < t_{m+1}$, namely the time interval before and after the switching action of leg *k*. Then, the relationship in (5) can hold true during the whole switching period *T*, when *k* takes the value from 0 to $N-1$.

REFERENCES

[1] D. J. Rogers and P. Lakshmanan, "Low-inductance snubber arrays for high-power, high-bandwidth switch-mode amplifiers," in *Proc. Appl. Power Electron. Conf. Expo.*, 2015, pp. 2557–2564.

[2] H. Ertl, J. W. Kolar, and F. C. Zach, "Analysis of a multilevel multicell switch-mode power amplifier employing the "flying-battery" concept," *IEEE Trans. Ind. Electron.*, vol. 49, no. 4, pp. 816–823, Aug. 2002.

[3] K. Nielsen, "Parallel phase-shifted carrier pulse-width modulation (PSCPWM)-a novel approach to switching power amplifier design," presented at the *102nd AES Conv.*, Munich, Germany, Mar. 1997, Paper 4447.

[4] D. Holmes and T. Lipo, *Pulse Width Modulation for Power Converters: Principles and Practice*, vol. 45. Hoboken, NJ, USA: Wiley, 2003, no. 1, pp. 71–77.

[5] S. H. Yang *et al.*, "A low-THD class-D audio amplifier with dual-level dual-phase carrier pulsewidth modulation," *IEEE Trans. Ind. Electron.*, vol. 62, no. 11, pp. 7181–7190, Nov. 2015.

[6] H. Liu, D. Zhang, and D. Wang, "Design considerations for output capacitance under inductance mismatches in multiphase buck converters," *IEEE Trans. Power Electron.*, vol. 32, no. 7, pp. 5004–5015, Jul. 2017.

[7] A. Kelly, "Current share in multiphase DC–DC converters using digital filtering techniques," *IEEE Trans. Power Electron.*, vol. 24, no. 1, pp. 212–220, Jan. 2009.

[8] O. Garcia, A. D. Castro, P. Zumelis, and J. A. Cobos, "Digital-control-based solution to the effect of nonidealities of the inductors in multiphase converters," *IEEE Trans. Power Electron.*, vol. 22, no. 6, pp. 2155–2163, Nov. 2007.

[9] J. A. Oliver, P. Zumel, O. Garcia, and J. A. Cobos, "Passive component analysis in interleaved buck converters," in *Proc. Appl. Power Electron. Conf. Expo.*, 2004, vol. 1, pp. 623–628.

[10] S. Chae, Y. Song, S. Park, and H. Jeong, "Digital current sharing method for parallel interleaved DC–DC converters using input ripple voltage," *IEEE Trans. Ind. Informat.*, vol. 8, no. 3, pp. 536–544, Aug. 2012.

[11] J. Gordillo and C. Aguilar, "A simple sensorless current sharing technique for multiphase DC–DC buck converters," *IEEE Trans. Power Electron.*, vol. 32, no. 5, pp. 3480–3489, May 2017.

[12] J. Han and J. H. Song, "Phase current-balance control using DC-link current sensor for multiphase converters with discontinuous current mode considered," *IEEE Trans. Ind. Electron.*, vol. 63, no. 7, pp. 4020–4030, Jul. 2016.

[13] P. D. Antoszczuk, R. G. Retegui, N. Wassinger, S. Maestri, M. Funes, and M. Benedetti, "Characterization of steady-state current ripple in interleaved power converters under inductance mismatches," *IEEE Trans. Power Electron.*, vol. 29, no. 4, pp. 1840–1849, Apr. 2014.

[14] M. Schuck and R. C. N. Pilawa-Podgurski, "Ripple minimization through harmonic elimination in asymmetric interleaved multiphase DC–DC converters," *IEEE Trans. Power Electron.*, vol. 30, no. 12, pp. 7202–7214, Dec. 2015.

[15] S. M. Cox, "Voltage and current spectra for a single-phase voltage source inverter," *IMA J. Appl. Math.*, vol. 74, no. 4, pp. 782–805, 2009.

[16] K. Nielsen, "Audio power amplifier techniques with energy efficient power conversion," Dept. Appl. Electron., Tech. Univ.Denmark, Lyngby, Denmark, Annu. Rep., 1998.

[17] M. Frigge, D. C. Hoaglin, and B. Iglewicz, "Some implementations of the Boxplot," *Amer. Statistician*, vol. 43, no. 1, pp. 50–54, 1989.

[18] Wolfspeed, Durham, NC, USA, C2M0080120D Datasheet, Nov. 19, 2015. [Online]. Available: www.wolfspeed.com.

[19] Wolfspeed, Durham, NC, USA, C4D30120D Datasheet, Oct. 11, 2016. [Online]. Available: www.wolfspeed.com.

[20] P. Cervellini, P. Antoszczuk, R. G. Retegui, and M. Funes, "Current ripple amplitude measurement in multiphase power converters," *IEEE Trans. Power Electron.*, vol. 32, no. 9, pp. 6684–6688, Mar. 2017.

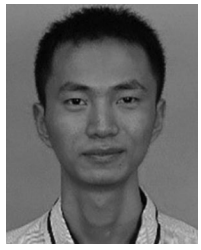

Xudong Wang (S'13) received the B.S. degree in electrical engineering in 2013 from Tsinghua University, Beijing, China, where he is currently working toward the Ph.D. degree in electrical engineering.

His current research interests include class-D power amplifiers and SiC devices.

Zhengming Zhao (M'02–SM'03–F'18) received the B.S. and M.S. degrees in electrical engineering from Hunan University, Changsha, China, in 1982 and 1985, respectively, and the Ph.D. degree from Tsinghua University, Beijing, China, in 1991.

In 1991, he joined the Department of Electrical Engineering, Tsinghua University. From 1994 to 1996, he was a Postdoctoral Fellow with The Ohio State University, Columbus, OH, USA, and then was a Visiting Scholar with the University of California, Irvine, CA, USA, for one year. He is currently a Professor with the Department of Electrical Engineering, Tsinghua University. His research interests include high-power conversion, power electronics and motor control, and solar energy applications.

Prof. Zhao is the Vice President of the Beijing Power Electronics Society and the Chairman of the IEEE Power Electronics Society Beijing Chapter.

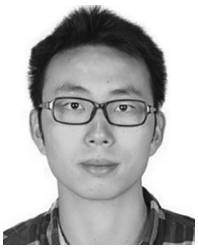

Kai Li (S'13–M'17) received the B.S. degree in electrical engineering from Wuhan University, Hubei, China, in 2011, and the Ph.D. degree from Tsinghua University, Beijing, China, in 2017.

From September 2013 to February 2015, he was a Visiting Scholar with the Center for Power Electronics Systems, Virginia Tech, Blacksburg, VA, USA. He is currently a Postdoctoral Fellow with the Department of Electrical Engineering, Tsinghua University. His research interests include modular multilevel converters and PWM strategies.

Kainan Chen (S'12–M'15) received the B.S. and Ph.D. degrees in electrical engineering from Tsinghua University, Beijing, China, in 2009 and 2014, respectively.

His current research interests include wireless power transfer, high-frequency power converter, and SiC devices.

Fang Liu (S'14) received the B.S. degree in electrical engineering from Sichuan University, Sichuan, China, in 2012. He is currently working toward the Ph.D. degree at the Department of Electrical Engineering, Tsinghua University, Beijing.

His research interests include wireless power transfer and PWM strategies.